symmetry

MDPI

Article

Nonlinear Coupled Equations Free-Boundary Problem in Atherosclerosis: Symmetry Analysis of Solutions and Numerical Simulation

Yarong Zhang [1,2,3], Xiaoya Mu [1], Xinyu Shi [1] and Jihuan He [1,4,5,*]

[1] School of Science, Xi'an University of Architecture and Technology, Xi'an 710055, China; yarong_zhang@xauat.edu.cn (Y.Z.); mu2498209813@xauat.edu.cn (X.M.); sxy2206050111@xauat.edu.cn (X.S.)
[2] Xi'an Special Equipment Inspection Institute, Xi'an 710061, China
[3] School of Power and Energy, Northwestern Polytechnical University, Xi'an 710129, China
[4] School of Jia Yang, Zhejiang Shuren University, Hangzhou 310015, China
[5] School of Mathematics and Big Data, Hohhot Minzu College, Hohhot 010010, China
* Correspondence: hejihuan@suda.edu.cn

Abstract: Atherosclerosis, a chronic inflammatory cardiovascular disease closely related to plaque formation during arteriosclerosis, poses a significant threat to global health. To deepen the understanding of the multifaceted interactions driving atherosclerosis progression and provide theoretical support for designing targeted therapeutic strategies, this study establishes a nonlinear coupled atherosclerotic free-boundary model integrating inflammatory immune cells, cytokines, and oxidized low-density lipoprotein. By applying the compression mapping principle, the local and global existence and uniqueness of solutions are proven, while revealing certain symmetries in the model's solution structure. Under specific assumptions, a quasi-steady-state approximate model is derived, and the existence of its solution is demonstrated. Through numerical simulations of the quasi-steady-state approximate model using the finite difference method, the temporal and spatial evolution of pro-inflammatory macrophages and oxidized low-density lipoprotein is analyzed. The findings highlight the model's strength in capturing the intricate dynamics of atherosclerosis, uncovering underlying mechanisms and identifying therapeutic targets. By evaluating inflammatory dynamics across plaque types and stenosis levels, the experimental design further validated the model's ability to replicate clinical processes and reinforced its predictive accuracy. Notably, in the process of model analysis and solution, symmetries in the equations and boundary conditions play a crucial role in determining the solution properties. However, the current one-dimensional model has limitations. Future research should focus on developing higher-dimensional models and integrating more influencing factors to enhance the model's clinical applicability and deepen the understanding of this complex disease.

Keywords: atherosclerosis; free-boundary problem; numerical simulation; mathematical modeling

check for updates

Academic Editor: Marek T. Malinowski

Received: 29 December 2024
Revised: 24 January 2025
Accepted: 26 January 2025
Published: 6 February 2025

Citation: Zhang, Y.; Mu, X.; Shi, X.; He, J. Nonlinear Coupled Equations Free-Boundary Problem in Atherosclerosis: Symmetry Analysis of Solutions and Numerical Simulation. *Symmetry* **2025**, *17*, 244. https://doi.org/10.3390/sym17020244

Copyright: © 2025 by the authors. Licensee MDPI, Basel, Switzerland. This article is an open access article distributed under the terms and conditions of the Creative Commons Attribution (CC BY) license (https://creativecommons.org/licenses/by/4.0/).

1. Introduction

Atherosclerosis, closely associated with cardiovascular diseases such as stroke and myocardial infarction, has become a global health concern. According to the Centers for Disease Control and Prevention (CDC), smoking, elevated levels of low-density lipoprotein (LDL), and hypertension are major risk factors contributing to the increased morbidity and mortality rates associated with this condition [1,2]. The pathogenesis of atherosclerosis is a

multi-stage process initiated by localized inflammation, leading to lipid and cellular debris accumulation, plaque formation, and potential luminal narrowing or occlusion. Plaque rupture can result in severe clinical events, such as myocardial infarction [3]. In recent years, research has extensively explored the regulatory roles of microRNAs in atherosclerosis and the applications of optical coherence tomography (OCT) and intravascular ultrasound (IVUS) for plaque monitoring [4,5]. Furthermore, novel PCSK9 inhibitors have been shown to significantly improve hyperlipidemia and atherosclerosis by upregulating LDLR protein levels [6]. For patients with symptomatic intracranial atherosclerotic stenosis, optimizing blood pressure management to maintain mean arterial pressure (MAP) has proven effective in reducing the risk of stroke [7]. HPDA/Zn nanoparticles stabilize plaques and enhance ultrasound imaging by inhibiting CREB activity [8]. Some models have investigated the role of high-density lipoprotein (HDL) in plaque formation [9], while reverse cholesterol transport (RCT) has been further elucidated through free-boundary models [10]. Numerical simulations have revealed that carotid artery stenosis significantly impacts the hemodynamics of the Willis circle, supporting assessments of cerebral vascular compensation mechanisms [11]. Additionally, studies have explored the effects of diabetes, vascular wall permeability, and inflammation propagation on atherosclerosis [12–14]. Simultaneously, mathematical modeling has played a crucial role in investigating the mechanisms of atherosclerosis, employing methods such as free-boundary models, partial differential equations, and bifurcation analysis. Researchers have utilized numerical simulations to evaluate plaque growth, hemodynamic changes, and the effects of therapeutic interventions, providing essential theoretical support for quantitative studies and treatment strategies for this disease [15–30].

Despite significant progress, current models have failed to effectively integrate the complex interplay of inflammation, lipid metabolism, and hemodynamics. This limitation restricts a comprehensive understanding of atherosclerosis and hinders the design of targeted therapeutic strategies. Thus, there is an urgent need for more advanced mathematical models to improve disease prediction and clinical management. Mathematical modeling, as a powerful tool in biomedical research, enables a quantitative understanding of complex biological processes. In the context of atherosclerosis, symmetry concepts play a pivotal role in capturing the inherent order and balance within the system. By identifying and incorporating symmetric relationships among key components, such as immune cells, cytokines, and lipoproteins, mathematical models can uncover the hidden patterns and mechanisms driving disease progression and development. This not only enhances the explanatory power of mathematical models but also provides a comprehensive framework for analyzing and predicting the behavior of atherosclerotic systems.

This study employs mathematical modeling to deeply explore the multidimensional interaction mechanisms in atherosclerosis progression and to provide theoretical support for targeted therapeutic strategies. The study constructs a nonlinear coupled free-boundary model that integrates key components such as inflammatory immune cells, cytokines, and oxidized low-density lipoproteins. In this process, previous research on control models, such as the free-boundary mathematical model of atherosclerosis proposed by Abi Younes et al., has provided the theoretical foundation for the development of this model [31]. The study rigorously proves the local and global existence and uniqueness of the model's solution, reveals its symmetry, and further derives a quasi-steady-state approximation model. Numerical simulations analyze the spatiotemporal evolution of key variables. Additionally, by combining the mathematical model with patient data, this study found that soft plaques and severe stenosis significantly increase pro-inflammatory macrophage activity and rupture risk, providing scientific evidence for identifying high-risk patients and developing treatment strategies. Numerical performance evaluation shows that, using macrophage

error as an example, as the grid density increases from 600 to 1200, the numerical error decreases from 1.28×10^{-5} to 2.83×10^{-6}. The convergence rate is consistent with theoretical second-order accuracy, validating the model's stability and reliability. Optimization methods, such as adaptive mesh refinement or GPU acceleration, can further improve computational efficiency, providing stronger support for the study of complex systems.

In conclusion, this study aims to capture the complex dynamic mechanisms of atherosclerosis, uncover potential pathological mechanisms, identify possible therapeutic targets, and provide direction for future high-dimensional modeling and the integration of additional influencing factors (such as hemodynamics and other risk factors), thereby further enhancing the clinical applicability of the model.

2. Mathematical Model of Atherosclerosis

Atherosclerosis is a complex physiological and pathological phenomenon involving multiple interacting factors, including immune cells, cytokines, low-density lipoprotein (LDL), oxidized low-density lipoprotein (ox-LDL), high-density lipoprotein (HDL), free radicals, foam cells, glucose, and insulin, along with other critical substances. To gain deeper insights into this intricate process, a simplified strategy was adopted, prioritizing the core drivers and regulatory mechanisms of inflammation to streamline the model structure and focus on the key mechanisms. Based on this approach, a mathematical model was developed, incorporating immune cells (M), cytokines (C), and low-density lipoprotein (L) as the three critical elements within the inflammatory context. This model is mathematically described by a set of three nonlinear, time-dependent, coupled partial differential equations with specific boundary conditions.

2.1. Model Equations

The mathematical formulation of the model is presented as follows:

$$\frac{\partial M}{\partial t} = D_M \nabla^2 M + \frac{\mu_1 C}{1 + C/\varsigma_1} + \rho ML - \theta ML + \alpha L - \omega_1 M, \tag{1}$$

$$\frac{\partial C}{\partial t} = D_C \nabla^2 C + \frac{\mu_2 C}{1 + C/\varsigma_2} M - \omega_2 C, \tag{2}$$

$$\frac{\partial L}{\partial t} = D_L \nabla^2 L + \frac{\eta M}{1 + M/\varsigma_3} - \omega_3 L. \tag{3}$$

Herein, M, C, and L denote $M = M(x,t)$, $C = C(x,t)$, and $L = L(x,t)$, respectively. M symbolizes the concentration of pro-inflammatory macrophages and monocytes capable of differentiating pro-inflammatory macrophages. C represents the concentration of pro-inflammatory cytokines, while L represents the concentration of oxidized low-density lipoprotein.

Equation (1) plays a crucial role in depicting the intricate time-dependent variations in the concentrations of inflammatory monocytes and macrophages within the context of atherosclerosis. The term $D_M \nabla^2 M$ serves as a mathematical representation of the diffusion process of these cells. The fraction $\frac{\mu_1 C}{1+C/\varsigma_1}$ is designed to model the recruitment of inflammatory monocytes. Here, $\mu_1 C$ reveals a fascinating aspect of the biological process, where the monocytes themselves release cytokines that drive their own recruitment, demonstrating a self-enhancing mechanism. This positive feedback loop can significantly impact the progression of inflammation. The denominator $1 + C/\varsigma_1$ introduces the concept of saturation. As the concentration of cytokines C increases, the recruitment rate of monocytes does not increase indefinitely but instead reaches a saturation point. This saturation effect is crucial for maintaining a stable cellular response and preventing an excessively exuberant inflam-

matory reaction. The term ρML refers to the absorption of ox-LDL by pro-inflammatory macrophages. This process is critically important in the development of atherosclerosis. When macrophages take up ox-LDL, they can transform into foam cells, which are a key component of atherosclerotic plaques. This uptake mechanism is tightly regulated by the concentrations of macrophages (M) and ox-LDL (L), highlighting the interdependence of these factors in the disease process. Simultaneously, θML models the transformation of macrophages through endothelial adhesion molecules. This transformation can alter the function and behavior of macrophages, potentially enhancing their pro-inflammatory properties or facilitating their migration within the vascular wall. The presence of αL indicates that oxidized low-density lipoprotein has a significant influence on the system. It may act as a signaling molecule or a trigger for various cellular responses, promoting certain reactions or changes in cell behavior that contribute to the progression of atherosclerosis. Finally, $\omega_1 M$ represents the breakdown of these inflammatory immune cells.

Equation (2) is specifically dedicated to comprehensively characterizing the temporal dynamics of pro-inflammatory cytokine concentrations. The diffusion of cytokines, represented by $D_C \nabla^2 C$, is an important factor in determining their distribution within the tissue. Similar to the diffusion of cells in Equation (1), cytokine diffusion is affected by the tissue structure and the presence of other molecules. The term $\frac{\mu_2 CM}{1+C/\varsigma_2}$ describes the secretion of pro-inflammatory cytokines. Here, $\mu_2 C$ indicates that the presence of cytokines themselves can enhance their own secretion, creating a positive feedback loop. This auto-amplification mechanism can rapidly increase the concentration of cytokines in the local environment, further fueling the inflammatory response. The dependence on the concentration of pro-inflammatory macrophages, M, shows that the interaction between macrophages and cytokines is bidirectional. Macrophages can secrete cytokines, and the presence of macrophages can also stimulate cytokine production. The denominator $1 + C/\varsigma_2$ represents the suppression of cytokine release driven by anti-inflammatory mechanisms. Finally, $\omega_2 C$ corresponds to the natural decomposition of cytokines. Degradation helps control the overall level of cytokines in the system. If cytokines were not degraded, their concentrations would continuously rise, leading to severe tissue damage and chronic inflammation. The degradation rate, ω_2, is influenced by various factors, such as the activity of enzymes and the presence of specific receptors that can clear cytokines from the system.

Equation (3) focuses on the detailed temporal dynamics of ox-LDL concentration. The term $D_L \nabla^2 L$ represents the diffusion of ox-LDL within the domain. This diffusion process determines how ox-LDL spreads throughout the tissue and interacts with other components. The term ηM indicates that the oxidation of LDL is closely related to the presence of macrophages. Macrophages can release reactive oxygen species and other mediators that can oxidize LDL. This oxidation process is a key step in the development of atherosclerosis as it converts native LDL into a more atherogenic form. The fraction $1 + M/\varsigma_3$ represents the uptake of ox-LDL by pro-inflammatory macrophages. The parameter ς_3 is related to the time required for macrophages to engulf ox-LDL. This uptake process is a critical event in the formation of atherosclerotic plaques. The efficiency of uptake depends on the concentrations of macrophages and ox-LDL, as well as the biological activity of macrophages. Finally, $\omega_3 L$ represents the breakdown of LDL particles via HDL-mediated reverse cholesterol transport. HDL plays a protective role in atherosclerosis by facilitating the removal of cholesterol from the arterial wall. The degradation of LDL particles by this mechanism helps to maintain the lipid balance within the tissue and reduce the risk of plaque formation. Understanding this process is essential for developing strategies to treat and prevent atherosclerosis.

2.2. Boundary Conditions

The problem is considered within the interval $[0, l]$, where l exhibits a time-dependent size $l(t)$. The boundary conditions are specified below:

$$\begin{cases} \frac{\partial M}{\partial x}(0,t) = 0, \frac{\partial M}{\partial x}(l(t),t) = \frac{\alpha_1+\mu_1 C}{1+C/\varsigma_1}, \\ \frac{\partial C}{\partial x}(0,t) = \frac{\partial C}{\partial x}(l(t),t) = 0, \\ \frac{\partial L}{\partial x}(0,t) = \frac{\partial L}{\partial x}(l(t),t) = 0. \end{cases} \tag{4}$$

For the concentration of pro-inflammatory macrophages, M, we have $\frac{\partial M}{\partial x}(0,t) = 0$, which indicates that there is no flux of these macrophages across the left boundary. At the right boundary, $x = l(t)$, we have $\frac{\partial M}{\partial x}(l(t),t) = \frac{\alpha_1+\mu_1 C}{1+C/\varsigma_1}$. This condition relates the gradient of M at the moving boundary to the concentrations of cytokines, C, and other factors. It implies that the change in the concentration of macrophages at the boundary is influenced by the local cytokine concentration and the recruitment mechanism modeled by the fraction $\frac{\mu_1 C}{1+C/\varsigma_1}$. For the concentration of pro-inflammatory cytokines, C, at both the left boundary, $x = 0$, and the right boundary, $x = l(t)$, we have $\frac{\partial C}{\partial x}(0,t) = \frac{\partial C}{\partial x}(l(t),t) = 0$. This means that there is no net flow of cytokines across the boundaries, suggesting that the cytokine concentration is not affected by external sources or sinks at the boundaries of the domain under consideration. Similarly, for the concentration of oxidized low-density lipoprotein, L, $\frac{\partial L}{\partial x}(0,t) = \frac{\partial L}{\partial x}(l(t),t) = 0$. This indicates that the diffusion of ox-LDL is also restricted at the boundaries, and there is no significant influx or efflux of ox-LDL across the boundaries of the domain.

These boundary conditions play a crucial role in determining the behavior of the solutions to the model equations within the domain and are essential for accurately simulating the atherosclerotic process.

2.3. Free-Boundary Movement Condition

The following condition is considered for the time-dependent variation of the free boundary:

$$\frac{dl}{dt} = -k_1 \left(\frac{\partial M}{\partial x}(l(t),t) + k_2 \frac{\partial L}{\partial x}(l(t),t) \right). \tag{5}$$

This condition implies that the rate of change of the free boundary is proportional to the gradient of the concentrations of pro-inflammatory macrophages and oxidized low-density lipoprotein and acts in the opposite direction. It characterizes the distribution and evolution of these concentrations on the boundary.

3. Local Existence and Uniqueness of the Solution

This section provides a detailed analysis to prove the local existence and uniqueness of the solution for the previously described atherosclerotic mathematical model. This requires a series of intricate mathematical manipulations and the application of fundamental mathematical principles.

3.1. Preliminary Arrangements and Assumptions

The first step is to organize and simplify the equations in the atherosclerotic mathematical model. Equations (1)–(5) need to be reformulated into a form suitable for analysis.

$$\begin{cases} M_t - D_M\nabla^2 M = \frac{\mu_1 C}{1+C/\varsigma_1} + \rho ML - \theta ML + \alpha L - \omega_1 M, t > 0, x \in (0, l(t)), \\ C_t - D_C\nabla^2 C = \frac{\mu_2 CM}{1+C/\varsigma_2} - \omega_2 C, t > 0, x \in (0, l(t)), \\ L_t - D_L\nabla^2 L = \frac{\eta M}{1+M/\varsigma_3} - \omega_3 L, t > 0, x \in (0, l(t)), \\ \frac{dl}{dt} = -k_1 \frac{\partial M}{\partial x}(l(t), t), l(0) = l_0, t > 0, \\ \frac{\partial M}{\partial x}(l(t), t) = \frac{\alpha_1+\mu_1 C}{1+C/\varsigma_1}, \frac{\partial C}{\partial x}(l(t), t) = 0, \frac{\partial L}{\partial x}(l(t), t) = 0, t > 0, \\ M(x, 0) = M_0(x), C(x, 0) = C_0(x), L(x, 0) = L_0(x), 0 \le x \le l_0. \end{cases} \tag{6}$$

The initial conditions are defined as non-negative, non-trivial functions to ensure the well-posedness of the problem. Specifically, $M_0(x), C_0(x)$, and $L_0(x)$ represent the initial concentrations of macrophages, cytokines, and oxidized low-density lipoproteins, respectively. These functions are non-negative, smooth, and bounded. Taking $L_0(x)$ as an example, it is continuously differentiable and satisfies the boundedness condition $L_0(x) \le L_{\max}$, where $L_{\max}$ is a positive constant. These properties are essential for ensuring the existence and uniqueness of solutions within the defined domain. Furthermore, the initial conditions satisfy the following properties:

$$M_0, C_0, L_0 \in C^2([0, l_0]), M_0(x), C_0(x), L_0(x) > 0, M(l_0), C(l_0), L(l_0) = 0, x \in (0, l_0). \tag{7}$$

3.2. Theorem Statement and Associated Estimates

Theorem 1. *This posits that condition (7) is fulfilled by M_0, C_0, and L_0, for any specified time interval $[0,\ T]$ (where T is a positive constant), and there exists a unique solution (M, C, L, l) to the problem (6). In addition to this theorem, the following estimates hold: Let $E(t)$ be an energy function related to the solution (the specific form of $E(t)$ can be referenced from the format in Theorem 1.1. (ii) of [32]). Thus, a constant C exists, depending only on the initial conditions and α (a number between 0 and 1), such that $E(t) \le C$ for all $(x, t) \in (0, l(t)) \times (0, T]$.*

3.3. Proof of Theorem

3.3.1. Transformation of the Free-Boundary Problem

Employing a method from the relevant reference (e.g., [32]), the free boundary is transformed into a fixed boundary. A smooth function, $\xi(x, t)$ (satisfying $\xi \in C^3(0, +\infty)$), is defined to ensure the smoothness and consistency of the boundary across different regions, such as $\xi(y) = 1$ for $y - l_0 < \frac{l_0}{4}$, $\xi(y) = 0$ for $y - l_0 > \frac{l_0}{2}$, and $|\xi'(y)| \le \frac{6}{l_0}$. The transformation $x = y + \xi(y)(l(t) - l_0)$ maps the dynamically changing free boundary onto a fixed boundary. This transformation simplifies the geometric complexity of the boundary, ensures the smoothness and physical consistency of the model, and facilitates further mathematical analysis. Let $x = \varphi(\xi, t)$, then φ is a differential homeomorphism from $(0, l_0)$ (where l_0 is the initial length of the domain) to $(0, l(t))$. Through direct calculation, expressions for the transformed equations can be obtained. For instance, substituting $x = \varphi(\xi, t)$ into the original equations yields equations in terms of ξ and t. Let $u(\xi, t) = M(\varphi(\xi, t), t)$, $v(\xi, t) = C(\varphi(\xi, t), t)$, and $w(\xi, t) = L(\varphi(\xi, t), t)$. As a result, the free-boundary problem (6) is converted into a problem in terms of u, v, and w with a fixed boundary in $(\xi, t) \in (0, l_0) \times (0, T]$.

3.3.2. Definition of a Set and Its Properties

Define $\Omega = \{(u, v, w, l) \in X : \|(u, v, w, l)\| \le R\}$, where X is a suitable function space (such as a *Sobolev* space) and R is a positive real number chosen appropriately. It is evident that Ω is a bounded and convex set.

3.3.3. Application of the Compression Mapping Principle

Firstly, due to the properties of φ, for any given $(u, v, w, l) \in \Omega$, the transformation $x = \varphi(\xi, t)$ is a differential homeomorphism. For any $(u, v, w, l) \in \Omega$, define a

mapping $F(u,v,w,l) = (F_1(u,v,w,l), F_2(u,v,w,l), F_3(u,v,w,l), F_4(u,v,w,l))$ as follows: $F_1(u,v,w,l)$ is obtained by substituting u, v, w, and l into the transformed equation for u(similarly for F_2, F_3, and F_4). By exploiting the *Sobolev* embedding theorem [33] and parabolic equation L^P estimates [34], it can be demonstrated that for any $(u,v,w,l) \in \Omega$, $F(u,v,w,l) \in \Omega$. That is, F maps Ω to itself. Moreover, to prove that F is a contraction mapping for suitably small values of a certain parameter (e.g., T or a coefficient in the equations), let $\Delta u = u_1 - u_2$, $\Delta v = v_1 - v_2$, $\Delta w = w_1 - w_2$, and $\Delta l = l_1 - l_2$, where (u_1, v_1, w_1, l_1) and (u_2, v_2, w_2, l_2) are two elements in Ω. Substituting (u_1, v_1, w_1, l_1) and (u_2, v_2, w_2, l_2) into the equations for F and taking the difference, we obtain equations for $\Delta F_1 = F_1(u_1, v_1, w_1, l_1) - F_1(u_2, v_2, w_2, l_2)$(similarly for ΔF_2, ΔF_3, and ΔF_4). Lastly, utilizing the L^P estimates of parabolic equations and the *Sobolev* embedding theorem, there exists a constant k (which depends on the initial data and the coefficients in the equations), such that $\|\Delta F(u,v,w,l')\| \leq k\|\Delta(u,v,w,l')\|$, where $\|\cdot\|$ is a suitable norm in the function space X. This indicates that F is a compression mapping on Ω.

3.3.4. Conclusions

According to the contraction mapping principle, there exists a unique fixed point (u,v,w,l) in Ω. By applying the L^P estimates and the Sobolev embedding theorem, we can determine the regularity of the solution of problem (6). That is, the functions u, v, w, and l possess certain smoothness and boundedness properties. Then, the original functions $M(x,t) = u(\varphi^{-1}(x,t),t)$, $C(x,t) = v(\varphi^{-1}(x,t),t)$, $L(x,t) = w(\varphi^{-1}(x,t),t)$, and l constitute the unique local solution of the free-boundary problem. Thus, the proof is complete.

4. Global Existence and Uniqueness of the Solution

This section aims to establish the global existence and uniqueness of the solution for the previously introduced atherosclerotic mathematical model. Achieving this requires a more detailed analysis than the proof of local existence and uniqueness.

4.1. Lemma and Its Significance

Lemma 1. *Let $M(x,t)$, $C(x,t)$, and $L(x,t)$ be the solutions to the free-boundary problem (6) within $(0,l(t)) \times (0,T]$, where T represents any positive real number and $l(t)$ denotes the time-varying length of the domain. There exist positive constants $C_i (i = 1,2)$, independent of T, such that:*

1. *There exists an inequality involving $M(x,t)$, $C(x,t)$, and $L(x,t)$. For example, $M(x,t)$, $C(x,t)$, and $L(x,t)$ are within the bounded region $(0, C_1]$.*
2. *Another relevant inequality is that $l'(t)$ lies within the bounded region $(0, C_2]$.*
   The proof of this lemma is crucial because it provides a foundation for establishing the global properties of the solution.

Proof. Firstly, by using the strong extremum principle, we know that in the region $(0,l(t)) \times (0,T]$, since the functions satisfy problem (6), they possess specific properties. Moreover, by employing the comparison principle, we consider an initial value problem related to the equations, as follows:

$$\begin{cases} \bar{M} = \dfrac{\mu_1 \bar{C}}{1 + \bar{C}/\varsigma_1} + \rho \bar{M}\bar{L} - \theta \bar{M}\bar{L} + \alpha \bar{L} - \omega_1 \bar{M}, t > 0, \\ \bar{C} = \dfrac{\mu_2 \bar{C}}{1 + \bar{C}/\varsigma_2} \bar{M} - \omega_2 \bar{C}, t > 0, \\ \bar{L} = \dfrac{\eta \bar{M}}{1 + \bar{M}/\varsigma_3} - \omega_3 \bar{L}, t > 0, \\ \bar{M}(0) = \|M_0\|, \bar{C}(0) = \|C_0\|, \bar{L}(0) = \|L_0\|. \end{cases} \tag{8}$$

The solution to the problem can be expressed as $\left(\bar{M}(t), \bar{C}(t), \bar{L}(t)\right)$. Let $U(t) = \bar{M}(t) + \bar{C}(t) + \bar{L}(t)$, and $U(t)$ satisfies the initial condition:

$$U(0) = \|M_0\|_\infty + \|C_0\|_\infty + \|L_0\|_\infty, \tag{9}$$

and the following relationship:

$$U_t = \frac{\mu_1 \bar{C}}{1 + \bar{C}/\varsigma_1} + (\rho - \theta)\bar{M}\bar{L} + \alpha\bar{L} - \omega_1\bar{M} + \frac{\mu_2 \bar{C}}{1 + \bar{C}/\varsigma_2}\bar{M} - \omega_2\bar{C} + \frac{\eta\bar{M}}{1 + \bar{M}/\varsigma_3} - \omega_3\bar{L}. \tag{10}$$

By using the comparison principle, it can be concluded that $M(x,t)$, $C(x,t)$, and $L(x,t)$ are all within the bounded region $(0, C_1]$. Then, by applying $Hopf$ lemma, the construction of an auxiliary function, the maximum principle, and a series of calculations, we can derive inequalities for $l'(t)$. □

4.2. Main Theorem and Its Proof

Theorem 2. *This is of utmost significance as it pertains to the global existence and uniqueness of the solution to the free-boundary problem (6). To prove this theorem, we undertake a detailed and systematic analysis.*

Proof. Firstly, let $[0, T_{\max})$ represent the maximum time interval for which the solution exists. According to Theorem 1, we already know that $T_{\max} > 0$. Our primary goal is to rigorously demonstrate that $T_{\max} = \infty$. By Lemma 1, we can firmly conclude that positive constants C_1 and C_2 exist (both independent of any arbitrary point within $[0, T_{\max})$), such that certain inequalities hold for the key variables of the model. Specifically, the concentrations $M(x,t)$, $C(x,t)$, and $L(x,t)$ are bounded in the region $(0, C_1]$, and the time-dependent length $l'(t)$ is bounded in $(0, C_2]$. Moreover, during the proof process, we rely on the L^P estimates, which play a crucial role in providing valuable information about the behavior of the solution. Through the application of these estimates, we can infer that a positive constant, C_3, exists (which depends solely on the initial data), such that specific conditions are satisfied for all $t \in [t_0, T_{\max})$. Here, t_0 is an arbitrarily chosen point within the time interval $[0, T_{\max})$. Finally, using the method of contradiction, assume that $T_{\max} < \infty$. Based on the properties of the solution and the results obtained from the previous steps, we know that for problem (6) with $t = t_0$ as the initial time, it can be uniquely extended to $[t_0, T_{\max} + \delta)$ for some $\delta > 0$. However, this contradicts the initial assumption that $T_{\max}$ is the maximum time existence interval. Therefore, through this proof by contradiction, we can definitively conclude that $T_{\max} = \infty$. This implies that the solution to the free-boundary problem is globally unique and exists. □

This result has profound implications for our understanding of the atherosclerotic mathematical model. It provides a solid theoretical foundation for further investigations into the long-term behavior and stability of the system modeled by the equations. It also validates the robustness of the model in representing the complex physiological and pathological processes associated with atherosclerosis over an extended period.

5. Existence of Solutions to the Quasi-Steady-State Approximate Model

This section centers on the quasi-steady-state approximation of the atherosclerotic mathematical model and explores the existence of solutions to this approximate model.

5.1. Assumption and Model Simplification

In the pursuit of a more tractable analysis of the atherosclerotic mathematical model, we introduce a specific and strategically important assumption regarding the second equation of the model, which is responsible for describing the evolution of pro-inflammatory cytokines.

We posit that, within the context of this equation, the diffusion term, denoted as $D_C\nabla^2 C$, does not exert a dominant influence on the overall behavior of cytokine concentration over time. This assumption is based on a comprehensive consideration of the biological and physical processes involved. In many real-world scenarios related to atherosclerosis, the impact of cytokine diffusion may be relatively minor compared to other factors, such as the production and consumption rates of cytokines in the local microenvironment. Consequently, under this assumption, we can justifiably simplify the equation by omitting the $D_C\nabla^2 C$ term. This simplification leads to a significant reduction in the complexity of the equation and allows us to focus more intently on the key relationships between the remaining variables. After making this simplification, the second equation can be rewritten in the form of a functional relationship between M and C. We denote this relationship as $C = f(M)$, where f represents a function that needs to be determined through subsequent mathematical operations. This new formulation not only streamlines the model but also opens up new avenues for in-depth analysis of the interdependencies among the variables involved in the atherosclerotic process.

By reducing the complexity of the model in this way, we are better equipped to study the essential characteristics of the system and gain valuable insights into the underlying mechanisms of atherosclerosis. This simplification step is a crucial part of our overall approach to understanding the complex dynamics of the disease through mathematical modeling.

5.2. Determining the Function $f(M)$

To find $f(M)$, we substitute $C = f(M)$ into the remaining terms of the second equation (after ignoring the diffusion term). We get

$$0 = \frac{f(M)\mu_2 M}{1 + f(M)/\varsigma_2} - f(M)\omega_2. \tag{11}$$

This is a quadratic equation in $f(M)$. We can solve this quadratic equation to find $f(M)$.

$$f(M) = \frac{\varsigma_2(\mu_2 M - \omega_2)}{\omega_2}. \tag{12}$$

5.3. Substitution into the Original System

Firstly, We substitute this expression for $C = f(M)$ into the first and third equations of the original system. For example, substituting into Equation (1), we get a new equation in terms of M and L only (after substituting $C = f(M)$). Similarly, substituting into Equation (3), we get another equation in terms of M and L. Then, by combining Equations (4) and (5) and substituting $C = f(M)$, we derive new expressions for $\frac{dl}{dt}$ and $\frac{\partial M}{\partial t}$ at $(l(t), t)$. We now have a system of two equations in two variables (M and L). We can study the existence of the solution to this reduced system, as follows:

$$\begin{cases} \frac{\partial M}{\partial t} = D_M\nabla^2 M + \frac{\mu_1 f(M)}{1+f(M)/\varsigma_1} + \rho ML - \theta ML + \alpha L - \omega_1 M, \\ \frac{\partial L}{\partial t} = D_L\nabla^2 L + \frac{\eta M}{1+M/\varsigma_3} - \omega_3 L, \\ \frac{dl}{dt} = -k_1\frac{a_1+b_1 M(l(t),t)}{a_2+b_2 M(l(t),t)}, \\ \frac{\partial M}{\partial x}(l(t),t) = \frac{a_1+b_1 M}{a_2+b_2 M}, \frac{\partial M}{\partial x}(0,t) = \frac{\partial L}{\partial x}(0,t) = \frac{\partial L}{\partial x}(l(t),t) = 0, \end{cases} \tag{13}$$

where

$$a_1 = \omega_2\varsigma_1(\alpha_1 - \mu_1\varsigma_2), b_1 = \varsigma_1\varsigma_2\mu_1\mu_2, a_2 = (\varsigma_1 - \varsigma_2)\omega_2, b_2 = \mu_2\varsigma_2. \quad (14)$$

5.4. Existence of Solution

According to the proof of Theorem 3.4 in reference [31], the quasi-steady-state approximate model (13) has the solution. This might involve showing that a certain mapping related to the equations is well-defined and has a fixed point, or using other methods such as the contraction mapping principle or the Brouwer fixed point theorem [35], depending on the nature of the equations.

6. Numerical Simulation

This section emphasizes the numerical simulation of the quasi-steady-state approximate model. We also take into account the potential symmetry-breaking factors during the discretization process. For example, the choice of numerical method might introduce small perturbations that could potentially disrupt the symmetric properties of the original model. To mitigate this, we carefully analyze the error propagation patterns related to symmetry and implement appropriate correction techniques. This ensures that the numerical results faithfully represent the symmetric nature of the underlying physical processes as much as possible.

6.1. Simulation Setup

We consider the quasi-steady-state approximate model obtained from the original atherosclerotic mathematical model. This model typically involves two or more variables whose evolution over time and space is of interest. For example, we might consider the concentrations of pro-inflammatory macrophages (M) and oxidized low-density lipoprotein (L). A numerical method, such as the finite difference method, is employed to discretize the equations of the quasi-steady-state approximate model. This involves dividing the spatial domain into a grid of points and approximating the derivatives in the equations using finite differences.

6.2. Simulation Results Variable Evolution

6.2.1. Time and Space Evolution

We simulate the temporal and spatial evolution of the variables (e.g., L and M). As illustrated in the Figures 1–3 below, we observe how the concentrations of pro-inflammatory macrophages and oxidized low-density lipoprotein vary over time and space.

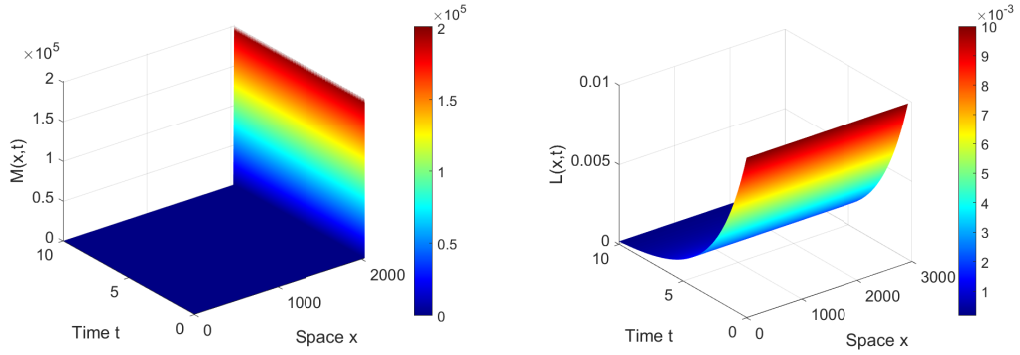

Figure 1. The evolution is shown when $D_M = 0.2$, $D_L = 0.1$, $\alpha = 0.00002$, $\alpha_1 = 2$, $\mu_1 = 0.000002$, $\mu_2 = 0.000002$, $\theta = 0.02$, $\omega_1 = 0.4$, $\omega_2 = 0.4$, $\omega_3 = 0.2$, $\varsigma_1 = 1$, $\varsigma_2 = 1$, $\varsigma_3 = 1$, $\eta = 0.00002$, $\rho = 0.000002$. We can see that, as time progresses, the concentrations vary in a certain pattern across the spatial domain.

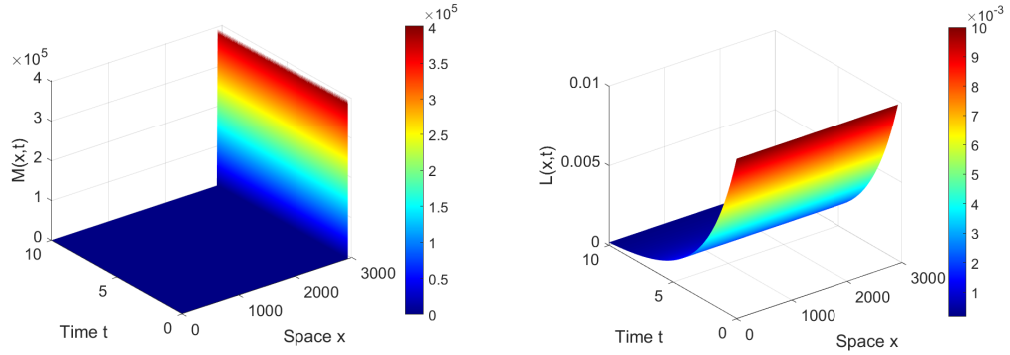

Figure 2. The scenario changes when $D_M = 0.4$, $D_L = 0.2$, $\alpha = 0.00004$, $\alpha_1 = 4$, $\mu_1 = 0.000004$, $\mu_2 = 0.000004$, $\theta = 0.04$, $\omega_1 = 0.8$, $\omega_2 = 0.8$, $\omega_3 = 0.4$, $\varsigma_1 = 2$, $\varsigma_2 = 2$, $\varsigma_3 = 2$, $\eta = 0.00004$, $\rho = 0.000004$. Here, the evolution of the concentrations is different from that in Figure 1, indicating the sensitivity of the model to different parameters or initial conditions.

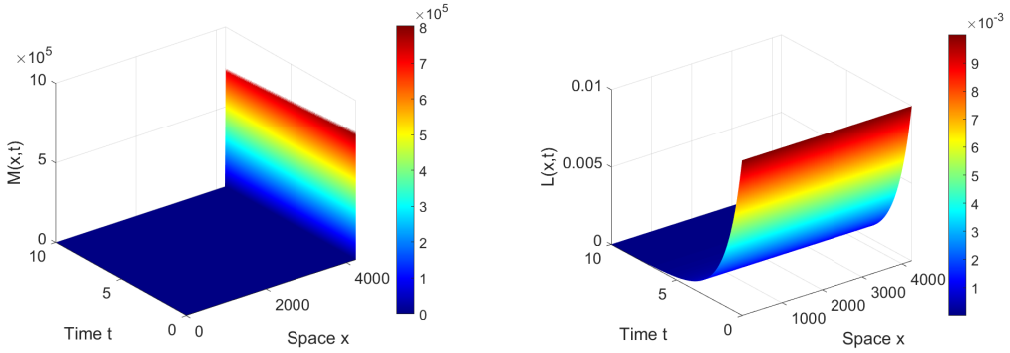

Figure 3. Another scenario when $D_M = 0.8$, $D_L = 0.4$, $\alpha = 0.00008$, $\alpha_1 = 8$, $\mu_1 = 0.000008$, $\mu_2 = 0.000008$, $\theta = 0.08$, $\omega_1 = 1.6$, $\omega_2 = 1.6$, $\omega_3 = 0.8$, $\varsigma_1 = 4$, $\varsigma_2 = 4$, $\varsigma_3 = 4$, $\eta = 0.00008$, and $\rho = 0.000008$. The patterns of concentration evolution continue to vary, highlighting the complexity of the system.

6.2.2. Effect of Parameters

The comparison of simulation results reveals that, as these parameters increase exponentially, the system exhibits more intense dynamic responses: the peak concentrations of inflammatory factors and ox-LDL rise significantly, and spatial distribution gradients become steeper. Furthermore, the system exhibits high sensitivity to parameter variations and initial conditions, with slight changes in parameter values resulting in markedly different dynamic outcomes. This sensitivity and nonlinear behavior highlight the strong coupling between variables and the complex dynamic interactions within the system. Overall, the diffusion coefficients accelerate the spatial propagation of substances, the time scales regulate the system's response speed, and the degradation rates balance the accumulation of substances. By adjusting these parameters appropriately, the system exhibits diverse nonlinear dynamic behaviors under different conditions, including spatial heterogeneity, rapid temporal responses, and changes in steady-state concentrations. These results illustrate the system's pronounced nonlinearity and complexity under high parameter values, uncovering the evolutionary patterns of inflammation and oxidation processes in both spatial and temporal dimensions. In cases of smaller parameter values (as shown in Figure 1), the system demonstrates relatively smooth dynamic behavior, with slow increases in the concentrations of inflammatory factors and ox-LDL, and spatial diffusion remaining relatively uniform. However, as parameters increase exponentially (as shown in Figures 2 and 3), the system's dynamic responses become progressively more intense, with significantly higher concentration peaks, faster evolution, and spatial heterogeneity.

In summary, diffusion coefficients govern the spatial propagation speed of substances, time scales regulate the response speed of the system, and degradation rates mitigate and balance substance accumulation. The interplay of these parameters results in diverse dynamic behaviors under different parameter conditions, including spatial heterogeneity, nonlinear temporal acceleration, and variations in steady-state concentrations.These findings highlight the sensitivity and complex evolutionary dynamics of inflammation and oxidation processes under varying conditions, further demonstrating the significant impact of parameter scaling on system dynamics.

6.2.3. Model Accuracy

To verify the reliability and effectiveness of the numerical method in solving the problem, numerical simulations were conducted again on the quasi-steady-state approximate model. The model's error, convergence, and numerical precision, along with its ability to effectively capture the dynamic behavior of the variables, were used to evaluate the model's accuracy. Numerical simulations were performed using MATLAB R2023a software on a personal computer equipped with an AMD Ryzen 5 3500U processor (2.10 GHz) and 8 GB of RAM. This configuration provides sufficient computational power and precision for the finite difference method and grid density analysis.

From Table 1 and its visualized results in Figure 4, it can be observed that the quasi-steady-state approximate model demonstrates favorable numerical properties under the finite difference method, including error reduction, improved convergence, and stable computational efficiency. As the grid density increases, the accuracy of the numerical solution improves, reflecting that higher-resolution grids can better capture the variations of the variables $M(x,t)$ and $L(x,t)$ in the model, thereby reducing numerical errors. This indicates that the finite difference method provides accurate numerical solutions and exhibits high applicability and reliability in solving such problems. In terms of convergence, the visual results show that, as the grid density increases, the convergence rate of the model gradually stabilizes, approaching the theoretical second-order accuracy. This convergence behavior is a key characteristic of the finite difference method, demonstrating that the numerical results are not only accurate but also that the numerical method is well-designed, allowing the solution to reliably approach the exact solution as the grid is refined. Furthermore, from an overall trend perspective, although the accuracy and convergence improve with increasing grid density, this improvement comes at the cost of increased computational effort. As the grid becomes finer, the time required for numerical computation increases, which reflects the trade-off between accuracy and computational cost commonly seen in the finite difference method. To address these limitations in computational efficiency, potential improvements can be explored. For example, adaptive mesh refinement techniques can dynamically allocate computational resources to areas with high variability, optimizing the balance between computational cost and accuracy. Additionally, leveraging modern computational techniques, such as parallel computing or GPU acceleration, could significantly reduce computation time while maintaining numerical precision. These methods provide feasible strategies to improve computational efficiency, particularly for scenarios requiring high-resolution and precise solutions.

In conclusion, the model solved using the finite difference method exhibits stable error convergence and high numerical accuracy, effectively capturing the dynamic behavior of the variables $M(x,t)$ and $L(x,t)$. As the grid density increases, the numerical solutions become progressively more accurate and the model's performance aligns with theoretical expectations, validating the reliability and effectiveness of the numerical method in addressing such problems. However, despite these strengths, the computational efficiency could be further optimized using advanced numerical techniques and computational resources.

Table 1. The quasi-steady-state approximate model was assessed based on convergence rate, numerical errors, and computational time with the application of finite difference methods.

Nx	Error M	Conv M	Error L	Conv L	CPU Time (s)
600	1.282863×10^{-5}	2.0100	7.267628×10^{-4}	2.0533	0.0866
800	7.024629×10^{-6}	2.0935	3.947990×10^{-4}	2.1212	0.1007
1000	4.308786×10^{-6}	2.1904	2.410734×10^{-4}	2.2106	0.1138
1200	2.827813×10^{-6}	2.3099	1.577346×10^{-4}	2.3266	1.1248

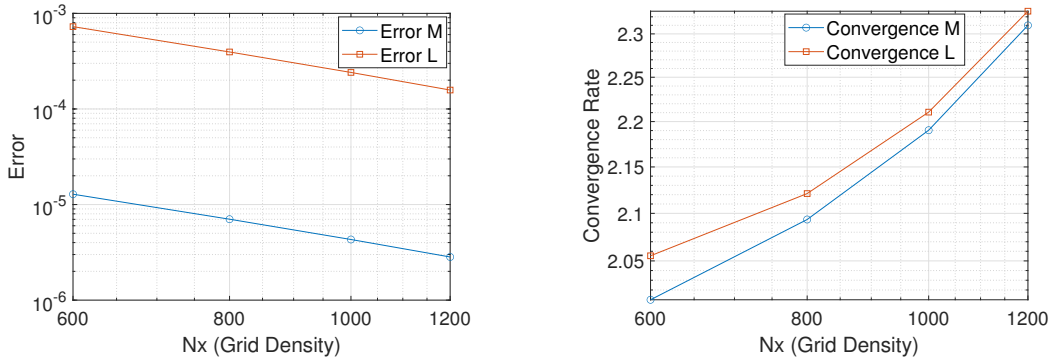

(**a**) Error vs. Grid Density (**b**) Convergence Rate vs. Grid Density

Figure 4. The errors of $M(x,t)$ and $L(x,t)$ vary with grid density and the convergence rate varies with grid density.

7. Experimental Design: Research on Stroke Risk Assessment Based on Carotid CT Angiography and Clinical Application

Purpose: This study integrates carotid artery CT angiography (CTA) with the quasi-steady-state approximate model; it investigates the dynamic impact of different plaque types (soft plaque, hard plaque, combined) and degrees of stenosis (mild, severe, combined) on pro-inflammatory immune cells, with the aim of exploring stroke risk assessment in patients with carotid stenosis. Methods: A total of 100 subjects underwent carotid artery CTA. Patients were positioned in the supine position, and routine scans were performed to identify lesion areas and scan levels. Plaque characteristics were classified based on CTA measurements by recording the number, location, and degree of carotid artery stenosis for each patient. To qualitatively illustrate changes in stroke risk across patient groups with varying stenosis severities and plaque types, numerical simulations based on the quasi-steady-state approximate model were conducted. The spatiotemporal distribution of $M(x,t)$ was established under three different conditions, and the changes in the color region range in the resulting numerical plots were analyzed to assess stroke risk levels. Results: Different plaque types and stenosis severities significantly influence the spatiotemporal evolution of $M(x,t)$. In cases of mild stenosis and hard plaques, $M(x,t)$ concentration is lower, with more blue regions, indicating a lower risk of plaque rupture and stroke. In cases of severe stenosis and soft plaques, $M(x,t)$ concentration is higher, with more red and yellow regions, indicating a higher risk of plaque rupture and increased stroke risk. The combined results reflect the weighted characteristics of patient groups with soft plaques; hard plaques; mixed plaques; and mild, severe, and moderate stenosis. At this point, color transitions are smooth, with more green regions and a small amount of red, indicating a moderate risk of plaque rupture and stroke for patients. Conclusion: Carotid CT angiography can be combined with a mathematical model for the evolution analysis of pro-inflammatory macrophages concerning different plaque types and stenosis severities.

This approach can explore the risk of plaque rupture in different patient populations and thus assess the risk of stroke in patients.

7.1. Study Subjects and Ethical Standards

A retrospective analysis was conducted on 100 patients with carotid artery stenosis admitted to Anxi County Hospital from August 2021 to August 2022 [36]. Inclusion criteria: (1) meeting the diagnostic criteria for carotid artery stenosis [37]; (2) having undergone CTA examination with complete clinical data; (3) keeping in touch. Exclusion criteria: (1) patients with concurrent severe cardiovascular or cerebrovascular diseases other than carotid artery stenosis; (2) patients with severe coagulopathy or coagulation dysfunction; (3) patients with severe endocrine dysfunction; (4) patients with concurrent malignant tumors; (5) patients who self-administered antithrombotic drugs within the last 3 months. Based on whether or not the patients experienced a stroke, all study subjects were divided into a stroke group $(n = 42)$ and a non-stroke group $(n = 58)$. All study subjects were informed about the study and signed informed consent forms. The study was reviewed and approved by the hospital's ethics committee. The stroke group consisted of 23 males and 19 females, with an average age of (62.16 ± 8.27) years and an average body mass index (BMI) of (23.15 ± 1.89) kg/m^2. The non-stroke group consisted of 30 males and 28 females, with an average age of (63.04 ± 8.45) years and an average body mass index (BMI) of (22.98 ± 1.75) kg/m^2. Among the 100 study subjects who underwent CTA, the degrees of carotid stenosis were as follows: mild stenosis in 17%, moderate stenosis in 18%, and severe stenosis in 18%. Plaque characteristics: soft plaques in 21%, hard plaques in 28%, and mixed plaques in 28%.

7.2. Experimental Process

All 100 study subjects underwent carotid CTA examinations. Carotid CTA was performed using a PHILPS 64-slice CT scanner, with iodopromide injection as the contrast agent, administered via the antecubital vein. Patients were positioned supine, and a routine scan was performed to identify the lesion area and scanning layers. The number of plaques, plaque locations, degree of carotid stenosis, and the presence of collateral circulation were recorded for each patient. Plaque characteristics were classified based on CTA measurements. Percentage data on stenosis severity and plaque type were used to calculate weighted average parameters to assess the characteristics of the patient groups. As shown in Table 2, based on the different types of stenosis, the diffusion coefficient of the quasi-steady-state approximate model was adjusted accordingly. In cases of mild stenosis, pro-inflammatory macrophage activity is low and local inflammation is minimal, reflected in the model by a smaller diffusion coefficient. In cases of moderate stenosis, pro-inflammatory macrophage activity is moderate and local inflammation is moderate, reflected in the model by a moderate diffusion coefficient. In cases of severe stenosis, pro-inflammatory macrophage activity is high and local inflammation is significant, reflected in the model by a higher diffusion coefficient.

Table 2. Diffusion coefficients of different carotid artery stenosis levels in patients.

	Mild Stenosis	**Moderate Stenosis**	**Severe Stenosis**
D_M (m^2/s)	0.005	0.008	0.01
D_L (m^2/s)	0.0005	0.0008	0.001

Weighted diffusion coefficients were calculated to capture the characteristics of the patient populations to compare stroke risk with varying degrees of stenosis and overall stroke risk across patient groups.

$$D_M^{\text{avg}} = 0.00409\ \text{m}^2/\text{s}, D_L^{\text{avg}} = 0.000409\ \text{m}^2/\text{s}. \quad (15)$$

Clinically, plaques are classified into stable plaques (also referred to as "hard plaques") and unstable plaques (also referred to as "soft plaques"). As shown in Table 3, the reaction rate and diffusion speed in the quasi-steady-state approximate model were adjusted based on the different plaque types. In soft plaques, pro-inflammatory macrophage activity is high and local inflammation is significant, reflected in the model as a higher reaction rate. In mixed plaques, pro-inflammatory macrophage activity and local inflammation are moderate, leading to a moderate reaction rate in the model. In hard plaques, pro-inflammatory macrophage activity is low and local inflammation is minimal, resulting in a lower reaction rate in the model.

Table 3. Reaction rates of different plaque types in patients' carotid arteries.

	Soft Plaque	**Hard Plaque**	**Mixed Plaque**
$\alpha\ (\text{s}^{-1})$	0.12	0.05	0.08
$\mu_1\ (\text{s}^{-1})$	0.2	0.1	0.15
$\omega_3\ (\text{s}^{-1})$	0.02	0.01	0.015
$k_1\ (\text{m}^5/\text{mol}\cdot\text{s})$	0.05	0.02	0.03

To compare stroke risk with different plaque types and overall stroke risk across patient groups, weighted reaction rates were calculated to reflect the characteristics of the patient populations.

$$\alpha^{\text{avg}} = 0.0793\,\text{s}^{-1}, \mu_1^{\text{avg}} = 0.148\,\text{s}^{-1}, \omega_3^{\text{avg}} = 0.01405\,\text{s}^{-1}, k_1^{\text{avg}} = 0.0313\,\text{m}^5/\text{mol}\cdot\text{s}. \quad (16)$$

7.3. Experimental Results and Analysis

This study uses numerical methods to simulate the three-dimensional spatial activity distribution of pro-inflammatory macrophages. Higher macrophage activity corresponds to a more intense inflammatory response, leading to a higher risk of plaque rupture and, consequently, a higher stroke risk. According to this characteristic in conjunction with the quasi-steady-state approximate model, combined with results from data analysis and processing, numerical simulations were performed using parameters for soft and hard plaques, mild and severe stenosis, and the weighted parameters applied to the quasi-steady-state approximate model. The study conducted comparative experiments on pro-inflammatory macrophage activity levels across different plaque types and stenosis severities in various patient groups. The results further confirm that pro-inflammatory macrophage activity holds potential clinical value for stroke risk assessment in stroke patient populations.

Figures 5 and 6 show the spatiotemporal evolution of pro-inflammatory macrophages under different plaque types and stenosis severities. A large number of red areas indicates higher pro-inflammatory macrophage activity and a greater stroke risk, whereas a large number of green areas suggests a lower stroke risk. Gradual color changes, with more green and a small amount of red, reflect a moderate stroke risk. The comparison of results between different plaque types, degrees of stenosis, and patient groups is clearly observable in the figures. When considering the characteristics of the patient population, smoother

color transitions, such as more green and some red, suggest a moderate diffusion rate, with moderate risks of repair and rupture, leading to a moderate stroke risk. In cases of soft plaques and severe stenosis, pro-inflammatory macrophage activity is higher, resulting in stronger local inflammation and an increased risk of plaque rupture. This is reflected by more red and yellow areas, indicating a higher stroke risk compared to other patient groups. In cases of hard plaques and mild stenosis, pro-inflammatory macrophage activity is lower, resulting in reduced local inflammation and a lower risk of plaque rupture, reflected by more blue areas, indicating a lower stroke risk compared to other patient groups. The evolutionary trends in the figures clearly show the impact of different plaque types and stenosis severities on pro-inflammatory macrophage activity, as well as the relationship between cell concentration changes and stroke risk. These findings provide strong support for future clinical applications, particularly in early diagnosis and preventive interventions for high-risk stroke populations, where monitoring pro-inflammatory macrophage activity may serve as an important assessment indicator.

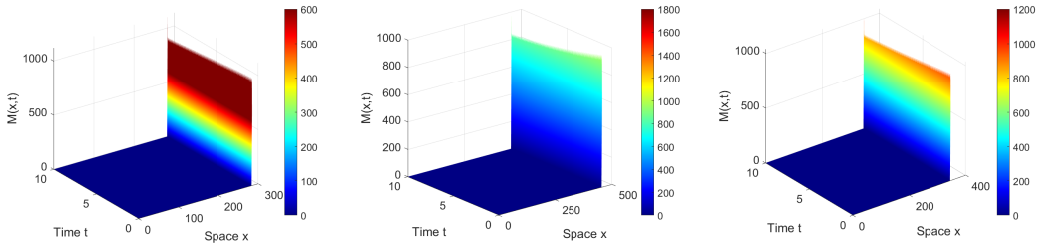

(**a**) Plaque Type: soft (**b**) Plaque Type: hard (**c**) Plaque Type: combined

Figure 5. The concentration of $M(x,t)$ over time and space was compared between soft, hard, and combined plaque types.

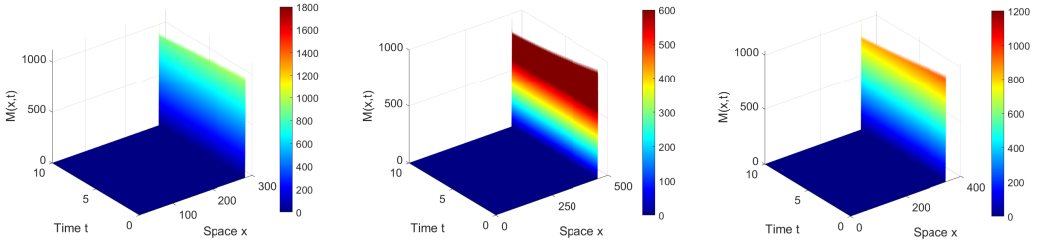

(**a**) Stenosis Level: mild (**b**) Stenosis Level: severe (**c**) Stenosis Level: combined

Figure 6. The concentration of $M(x,t)$ over time and space was compared between mild, severe, and combined stenosis levels.

7.4. Conclusions

In this study, we conducted an in-depth exploration of how soft and hard plaques, as well as different degrees of stenosis, affect the activity of pro-inflammatory macrophages in patients with carotid stenosis, using a mathematical model combined with data on plaque types and stenosis severity from the patient population. The results indicated that, in cases of soft plaques and severe stenosis, pro-inflammatory macrophage activity significantly increased, correlating with exacerbated local inflammatory responses and an elevated risk of plaque rupture. This heightened activity was evident in the image analysis, as shown by the increased presence of red and yellow areas. In contrast, under conditions of hard plaques and mild stenosis, pro-inflammatory macrophage activity was relatively low, indicating a weaker inflammatory response and greater plaque stability, which was shown by the presence of more blue areas in the images. By analyzing the clinical characteristics of the patient population, we found that smoother color transitions, such as more green areas, indicated a moderate spread of the inflammatory response, with moderate repair and

rupture risks. These findings provide new insights into the pathological mechanisms of carotid stenosis and offer important guidance for developing clinical treatment strategies. Monitoring pro-inflammatory macrophage concentration could help doctors identify high-risk patients earlier and adjust treatment plans accordingly, such as using anti-inflammatory drugs or adopting more aggressive interventions. Additionally, our research points to future directions, including exploring differences in inflammatory responses among patients with different genotypes and evaluating the long-term outcomes of various treatment strategies. Through these efforts, we hope to increase the success rate of treatment for patients with carotid stenosis, reduce the risk of complications, and ultimately improve patient quality of life. This study not only advances our understanding of the pathology of carotid stenosis but also provides a scientific basis for developing new treatment strategies and interventions, with the potential to reduce the incidence and mortality of carotid stenosis-related diseases in the future.

8. Summary and Outlook

This study employs a nonlinear coupled model with free-boundary conditions to explore the dynamic mechanisms of atherosclerosis, a chronic inflammatory cardiovascular disease. By integrating key elements such as inflammatory immune cells, cytokines, and oxidized low-density lipoprotein, the model captures the intricate dynamics of the disease process, providing new theoretical insights into its pathological mechanisms.

Symmetry plays a fundamental yet implicit role throughout the model's formulation and analysis. In the model equations, the interaction terms between different variables exhibit a certain degree of symmetry in their functional forms, which reflects the balanced and reciprocal relationships in the biological processes. For example, the recruitment term of inflammatory monocytes and the transformation terms of macrophages are structured in a way that shows a symmetrical dependence on the concentrations of related factors. In the boundary conditions, the zero-flux conditions for cytokines and oxidized low-density lipoprotein at the boundaries imply a symmetry in the spatial distribution of these substances within the domain, preventing any preferential accumulation or depletion at the edges.

The existence and uniqueness of solutions, both locally and globally, have been rigorously proven, ensuring the model's reliability as a foundation for studying atherosclerosis and exploring potential intervention strategies. The transformation of the free-boundary problem into a fixed boundary one and the application of the compression mapping principle rely on the underlying symmetric and topological properties of the model. These proofs not only establish the mathematical soundness of the model but also reveal the stability and determinacy of the atherosclerotic system it describes, making it a valuable tool for predicting disease progression and assessing the impact of therapeutic interventions. The quasi-steady-state approximate model, derived under reasonable assumptions, simplifies the analysis while retaining essential symmetric features, thereby facilitating practical computational implementations that can aid in understanding disease dynamics in realistic settings. Numerical simulations of the approximate model using the finite difference method provide valuable insights into the temporal and spatial evolution of key variables. These insights can help identify critical parameters influencing inflammatory responses, enabling targeted clinical interventions. The integration of experimental data on plaque types and stenosis severity further validates the model, emphasizing its applicability in replicating real-world pathological processes. The results show that increasing diffusion and reaction parameters intensifies the inflammatory response, and the model's sensitivity to these parameters highlights the nonlinear and symmetrically coupled nature of the

system, offering quantitative guidance for optimizing treatment strategies and modulating the biological pathways involved in atherosclerosis.

While the proposed model effectively captures the dynamics of atherosclerosis, it is not without limitations. The one-dimensional framework simplifies the inherent three-dimensional complexity of arterial walls, and it neglects the influence of hemodynamics on inflammation and plaque formation. Furthermore, critical risk factors such as hypercholesterolemia and diabetes are omitted, and the parameterization of the model relies heavily on experimental data, thereby constraining its generalizability and applicability. Future research should aim to integrate hemodynamic effects and additional risk factors to enhance the model's clinical relevance and capacity to comprehensively predict disease progression. Moreover, in such models, new symmetries related to the geometry and flow patterns of the artery can be incorporated. For example, the cylindrical symmetry of the artery can be exploited to simplify the model structure and improve computational efficiency. Meanwhile, also integrating other crucial factors such as various risk factors like high cholesterol, diabetes, and hypertension is essential. These factors can interact with the existing model components in a symmetric or asymmetric manner, and understanding these interactions will enhance the model's clinical applicability. Moreover, future extensions should explore models with data-driven techniques, such as machine learning, which can uncover novel insights into disease progression and refine parameter estimations and incorporate feedback mechanisms to simulate the effects of therapeutic interventions, such as anti-inflammatory treatments or cholesterol-lowering drugs, which could help assess the efficacy of different clinical strategies.

In conclusion, this study lays a solid foundation for further research in atherosclerosis modeling. By emphasizing the importance of symmetry and providing a detailed analysis of the model's properties and behaviors, it paves the way for more accurate and comprehensive models that can potentially contribute to improved diagnosis and treatment strategies for atherosclerosis. Future work integrating three-dimensional modeling, personalized parameterization, and real-time clinical feedback mechanisms will not only enhance the model's predictive capability but also establish a stronger connection to practical medical applications.

Author Contributions: Conceptualization, X.M. and J.H.; methodology, Y.Z., X.M. and X.S.; software, X.M.; validation, Y.Z., J.H. and X.S.; formal analysis, Y.Z.; investigation, Y.Z., X.M. and X.S.; resources, J.H.; data curation, X.S.; writing—original draft preparation, Y.Z. and X.M.; writing—review and editing, J.H. and X.S.; visualization, X.M.; supervision, J.H.; project administration, Y.Z.; funding acquisition, Y.Z. All authors have read and agreed to the published version of the manuscript.

Funding: We acknowledge the financial support from the National Natural Science Foundation of China (12101482), the Postdoctoral Science Foundation of China (2022M722604), the General Project of Science and Technology of Shaanxi Province (2023-YBSF-372), the Shaanxi Mathematical Basic Science Research Project (23JSQ042), and the Xi'an Science and Technology Plan Project (2024JH-GXFW-0064).

Data Availability Statement: Data are contained within the article.

Conflicts of Interest: The authors declare no conflicts of interest.

References

1. Mendis, S.; Puska, P.; Norrving, B. *Global Atlas on Cardiovascular Disease Prevention and Control*; World Health Organization: Geneva, Switzerland, 2011.
2. Virani, S.S.; Alonso, A.; Benjamin, E.J.; Bittencourt, M.S.; Callaway, C.W.; Carson, A.P.; Chamberlain, A.M.; Chang, A.R.; Cheng, S.; Delling, F.N.; et al. Heart disease and stroke statistics—2020 update: A report from the American Heart Association. *Circulation* **2020**, *141*, e139–e596. [CrossRef] [PubMed]
3. Ross, R. Atherosclerosis—An inflammatory disease. *N. Engl. J. Med.* **1999**, *340*, 115–126. [CrossRef] [PubMed]

4. Wei, Y.; Zhu, M.; Schober, A. Macrophage microRNAs as therapeutic targets for atherosclerosis, metabolic syndrome, and cancer. *Int. J. Mol. Sci.* **2018**, *19*, 1756. [CrossRef] [PubMed]
5. Lv, R.; Maehara, A.; Matsumura, M.; Wang, L.; Wang, Q.; Zhang, C.; Guo, X.; Samady, H.; Giddens, D.P.; Zheng, J.; et al. Using optical coherence tomography and intravascular ultrasound imaging to quantify coronary plaque cap thickness and vulnerability: A pilot study. *Biomed. Eng. Online* **2020**, *19*, 1–18. [CrossRef]
6. Wang, W.Z.; Liu, C.; Luo, J.Q.; Lei, L.J.; Chen, M.H.; Zhang, Y.Y.; Sheng, R.; Li, Y.N.; Wang, L.; Jiang, X.H.; et al. A novel small-molecule PCSK9 inhibitor E28362 ameliorates hyperlipidemia and atherosclerosis. *Acta Pharmacol. Sin.* **2024**, *45*, 2119–2133. [CrossRef]
7. Chen, Z.; Liu, J.; Wang, A.; Wu, B.; Cheng, Z.; Jiang, Y.; Gu, H.; Ding, L.; Mo, J.; Jiang, Y.; et al. Hemodynamic impairment of blood pressure and stroke mechanisms in symptomatic intracranial atherosclerotic stenosis. *Stroke* **2024**, *55*, 1798–1807. [CrossRef]
8. Chen, L.; Jiang, Z.; Yang, L.; Fang, Y.; Lu, S.; Akakuru, O.U.; Huang, S.; Li, J.; Ma, S.; Wu, A. HPDA/Zn as a CREB inhibitor for ultrasound imaging and stabilization of atherosclerosis plaque. *Chin. J. Chem.* **2023**, *41*, 199–206. [CrossRef]
9. Abi Younes, G.; El Khatib, N. Mathematical modeling of atherogenesis: Atheroprotective role of HDL. *J. Theor. Biol.* **2021**, *529*, 110855. [CrossRef]
10. Chen, Y.; Liu, W.; Zhao, Y. Bifurcation for a free boundary model of an atherosclerotic plaque formation in the presence of reverse cholesterol transport with Holling type III functional response. *Discret. Contin. Dyn. Syst. B* **2024**, *29*, 4194–4227. [CrossRef]
11. Sun, H.; Li, B.; Zhang, L.; Zhang, Y.; Liu, J.; Huang, S.; Xi, X.; Liu, Y. Numerical study of hemodynamic changes in the Circle of Willis after stenosis of the internal carotid artery. *Comput. Methods Programs Biomed.* **2024**, *243*, 107881. [CrossRef]
12. Xie, X. Steady solution and its stability of a mathematical model of diabetic atherosclerosis. *J. Biol. Dyn.* **2023**, *17*, 2257734. [CrossRef] [PubMed]
13. El Hajj, W.; El Khatib, N. Effect of permeability on the initiation of Atherosclerosis modeled as an inflammatory process. *J. Theor. Biol.* **2023**, *564*, 111461. [CrossRef] [PubMed]
14. El Hajj, W.; El Khatib, N.; Volpert, V. Inflammation propagation modeled as a reaction–diffusion wave. *Math. Biosci.* **2023**, *365*, 109074. [CrossRef] [PubMed]
15. Nasresfahani, F.; Eslahchi, M.R. Error analysis of finite difference/collocation method for the nonlinear coupled parabolic free boundary problem modeling plaque growth in the artery. *Appl. Math. Comput.* **2021**, *405*, 126221. [CrossRef]
16. Ahmed, I.U.; Myerscough, M.R. HDL and plaque regression in a multiphase model of early atherosclerosis. *Math. Biosci.* **2024**, *373*, 109208. [CrossRef] [PubMed]
17. Mukherjee, D.; Muni, S.S.; Fatoyinbo, H.O. A dynamical system framework for a mathematical model of atherosclerosis. *Frankl. Open* **2024**, *7*, 100116. [CrossRef]
18. Hernández-López, P.; Cilla, M.; Martínez, M.A.; Peña, E.; Malvè, M. Impact of geometric and hemodynamic changes on a mechanobiological model of atherosclerosis. *Comput. Methods Programs Biomed.* **2024**, *254*, 108296. [CrossRef]
19. Liu, Y. Mathematical modeling and simulation of atherosclerotic formation and progress at arterial bifurcations. *Biomed. Signal Process. Control* **2023**, *80*, 104266. [CrossRef]
20. Zhang, X.; Hu, B.; Zhang, Z. Bifurcation for a free-boundary problem modeling small plaques with reverse cholesterol transport. *J. Math. Anal. Appl.* **2023**, *517*, 126604. [CrossRef]
21. Soleimani, M.; Dashtbozorg, B.; Mirkhalaf, M.; Mirkhalaf, S.M. A multiphysics-based artificial neural networks model for atherosclerosis. *Heliyon* **2023**, *9*, e17902. [CrossRef]
22. Xie, X. Well-posedness of a mathematical model of diabetic atherosclerosis. *J. Math. Anal. Appl.* **2022**, *505*, 125606. [CrossRef] [PubMed]
23. Noble, C.; Carlson, K.D.; Neumann, E.; Lewis, B.; Dragomir-Daescu, D.; Lerman, A.; Erdemir, A.; Young, M.D. Finite element analysis in clinical patients with atherosclerosis. *J. Mech. Behav. Biomed. Mater.* **2022**, *125*, 104927. [CrossRef] [PubMed]
24. Ni, W.; Shi, J.; Wang, M. Global stability of spatially nonhomogeneous steady state solution in a diffusive Holling-Tanner predator-prey model. *Proc. Am. Math. Soc.* **2021**, *149*, 3781–3794. [CrossRef]
25. Kubugha, B.W.; Amos, E. Impact of treatment parameter on blood flow in an atherosclerotic artery. *Am. J. Theor. Appl. Stat.* **2020**, *9*, 74–79.
26. Xu, S.; Ilyas, I.; Little, P.J.; Li, H.; Kamato, D.; Zheng, X.; Luo, S.; Li, Z.; Liu, P.; Han, J.; et al. Endothelial dysfunction in atherosclerotic cardiovascular diseases and beyond: From mechanism to pharmacotherapies. *Pharmacol. Rev.* **2021**, *73*, 924–967. [CrossRef]
27. Malas, M. Application of transcarotid artery revascularization for carotid bifurcation atherosclerosis—The preferred stent-angioplasty option for vascular surgeons. In *Seminars in Vascular Surgery*; WB Saunders: Philadelphia, PA, USA, 2020; Volume 33, pp. 1–3.
28. Hao, W.; Friedman, A. The LDL-HDL profile determines the risk of atherosclerosis: A mathematical model. *PLoS ONE* **2014**, *9*, e90497. [CrossRef]

29. El Khatib, N.; Kafi, O.; Sequeira, A.; Simakov, S.; Vassilevski, Y.; Volpert, V. Mathematical modeling of atherosclerosis. *Math. Model. Nat. Phenom.* **2019**, *14*, 603. [CrossRef]
30. Liu, Y.P.; He, J.H. A fast and accurate estimation of amperometric current response in reaction kinetics. *J. Electroanal. Chem.* **2025**, *978*, 118884. [CrossRef]
31. Abi Younes, G.; El Khatib, N.; Volpert, V. A free boundary mathematical model of atherosclerosis. *Appl. Anal.* **2024**, *103*, 240–262. [CrossRef]
32. Wang, M. The existence and uniqueness of solutions of free boundary problems in heterogeneous environments. *Discret. Contin. Dyn.-Syst.-Ser. B* **2019**, *24*, 415–421. [CrossRef]
33. Adams, R.A.; Fournier, J.J.F. *Sobolev Spaces*; Elsevier: Amsterdam, The Netherlands, 2003.
34. Ladyzhenskaia, O.A.; Solonnikov, V.A.; Ural'tseva, N.N. *Linear and Quasi-Linear Equations of Parabolic Type*; American Mathematical Society: Providence, RI, USA, 1968.
35. Park, S. Ninety years of the Brouwer fixed point theorem. *Vietnam J. Math.* **1999**, *27*, 187–222.
36. Zheng, H.L. Value of carotid artery CTA combined with carotid Doppler ultrasound in assessing stroke risk in patients with carotid artery stenosis. *Mod. Med. Imaging* **2024**, *33*, 1405–1408.
37. Vascular Surgery Group of the Surgery Branch of the Chinese Medical Association. Guidelines for the Diagnosis and Treatment of Carotid Artery Stenosis. *Chin. J. Vasc. Surg. (Electron. Ed.)* **2017**, *9*, 169–175.

Disclaimer/Publisher's Note: The statements, opinions and data contained in all publications are solely those of the individual author(s) and contributor(s) and not of MDPI and/or the editor(s). MDPI and/or the editor(s) disclaim responsibility for any injury to people or property resulting from any ideas, methods, instructions or products referred to in the content.